Control mechanism of atomic ionization and high-order harmonic generation assisted by attosecond pulses

H. C. Lee · T. F. Jiang

Abstract Attosecond pulses combined with infrared laser constitute a powerful tool for controlling atomic photoionization and high-order harmonic generation (HHG). We apply the intense-field many-body S-matrix theory to solve such two-pulse excitation problems. The theory can give a clear explanation for the oscillation of ionization probability as a function of time delay between infrared field and attosecond pulses with central frequency lying below ionization threshold at moderate infrared intensities. The HHG assisted by such attosecond pulses is also interpreted. In addition to a known dramatic enhancement of HHG, a harmonic emission from rapid oscillation of bound-state population caused by the counter-rotating wave is presented.

1 Introduction

Attosecond pulses (attopulses) combined with infrared (IR) field are powerful tools in atomic ionization [1–5] and high-order harmonic generation (HHG) [6–8] through the control of time delay between the two fields. Among these applications, the property of attopulses with central frequency lying above or below the ionization threshold is critical. For the above-ionization (A.I.) attopulses, whose central frequency is above the ionization threshold, atomic photoionization is mainly accomplished by the attopulses via a one-photon process, while an IR field (usually weak) only streaks or perturbs the atomic states [9]. However, for the below-ionization (B.I.) attopulses, whose central frequency is below the threshold, the attopulses only pump ground-state electrons into excited bound states. An IR field becomes necessary to ionize these excited electrons as will be shown in Fig. 5b later.

Johnsson et al. [5] showed experimentally that the B.I. attopulses can be used to control ion yield by varying the phase difference between the attopulses and IR field. The ion yield oscillates at twice IR frequency and the modulation ratio can be as high as 35 %. The oscillation no longer exists when the A.I. attopulses are used. In general, the oscillation is regarded as the interference between bound electron wave packets (EWPs) created by a series of bursts of attopulses, which is also called the attosecond pulse train (APT). However, recent reports indicate that even a single attosecond pulse (SAP) or few-burst APT may also create such oscillation [10, 11].

Theoretically, the oscillation was studied by several groups based on the time-dependent Schrödinger equation (TDSE) calculations. For example, Tong et al. [10] explained the oscillation mechanism in the Floquet picture [12]. Peng et al. [13] showed a great IR effect on the photoionization even at a very weak intensity. Ranitovic et al. [14] showed that the resonant absorption of IR or APT is critical in the excitation. Without using TDSE calculation, Rivière et al. [15] used the three-step model [16, 17] to treat the IR field as an intense field. In this paper, we provide a semi-analytic approach based on the intense-field many-body S-matrix theory (IMST) proposed by Becker and Faisal [18]. With the IMST, the total Hamiltonian can be partitioned in suitable ways to handle the initial and final physical situations properly. As a result, the effect of APT and IR fields is decoupled, and each of them can be independently solved. The theory can explain the oscillation in a clear picture. The interference effect between EWPs excited by bursts of the APT is elucidated, and a robust oscillation generated by a few-burst APT or a few-cycle IR field can also be shown.

H. C. Lee (✉) · T. F. Jiang
Institute of Physics, National Chiao Tung University,
1001 University Road, Hsinchu 30010, Taiwan
e-mail: hclee@mail.nctu.edu.tw

Interestingly, we found another oscillation, caused by the counter-rotating wave (CRW), when the B.I. attopulses pump electrons from ground to higher bound states. In a two-state system, the CRW comes from the rapid oscillation terms of the Hamiltonian of $\Omega\{\exp[i(\omega_0 + \omega_L)t] + \exp[i(\omega_0 - \omega_L)t]\}|e><g| +$ h.c., and is usually neglected compared with the rotating wave (slow oscillation term), where ω_0 is the energy spacing between the excited $|e>$ and ground $|g>$ states, ω_L is the incident light frequency, Ω is the Rabi frequency and h.c. is Hermitian conjugate. With the case of helium excited by the B.I. attopulses constructed by 800 nm IR field, we show that the CRW can modulate the bound-state population with an oscillation as fast as 90 as. After an IR excitation, the rapid oscillation caused by the CRW can also give rise to the HHG, which is around 30 harmonic orders and has a high-order harmonic plateau. Because the HHG is not weak, it may provide a practical method to identify CRW. In addition to generating an evident CRW, the B.I. attopulses also lead the HHG to be dramatically enhanced [8, 19, 20] with a multi-channel recombination, which will be elucidated later. The remainder of this paper is organized as follows. In Sect. 2, we describe the theory (IMST) for (i) the atomic ionization and (ii) the HHG assisted by the B.I. attopulses. In Sect. 3, we interpret (i) the mechanism of ion-yield oscillation and (ii) the B.I. APT's effects on the HHG. Finally, conclusions are drawn in Sect. 4.

2 Theory

2.1 Atomic ionization

Unless otherwise specified, we use atomic units (a.u.) in this paper. According to the IMST [18], the total Hamiltonian can be partitioned in alternating ways to treat the physical situation properly. Initially, the physical system is dominated by the atomic potential and the APT field, and thus the total Hamiltonian is partitioned as

$$H(t) = H_i(t) + V_i(t), \tag{1}$$

where $H_i(t) = \mathbf{p}^2/2 + V_a(r) + V_{APT}(t)$. $V_a(r)$ is the atomic model potential within the single active electron (SAE) approximation [21]. $V_{APT}(t) = \mathbf{A}_{APT}(t) \cdot \mathbf{p}/c$ with $\mathbf{A}_{APT}(t) = -c \int_{-\infty}^{t} \mathbf{E}_{APT}(t')dt'$. $V_i(t) = V_{IR}$ is the interaction due to the IR field, and

$$\mathbf{E}_{APT}(t) = \hat{z} \sum_{\xi} (-1)^{\xi} E_x \sin[\omega_x(t - \xi T_h)]$$
$$\exp\left[-2\ln 2\left(\frac{t - \xi T_h}{\tau_x}\right)^2\right] \exp\left[-2\ln 2\left(\frac{t}{\tau_T}\right)^2\right], \tag{2}$$

where $E_x = 8.7 \times 10^7$ V/cm (intensity: $I_{APT} = 10^{13}$ W/cm^2). For the helium atom ($I_p = 24.6$ eV), we choose $\omega_x = 23$ eV, $\tau_x = 0.3\,fs$, $\tau_T = 5\,fs$ and $T_h = \pi/\omega_{IR}$, where I_p denotes the ionization potential from the 1s state. The dummy index ξ is an integer and summed from -10 to 10 for the case of many-burst APT. The method is applicable to other atomic targets with suitable model potentials and pulse parameters.

Let $|\varphi_i(t)>$ be the solution of $H_i(t)$. Then, the wave function $|\varphi_i(t)>$ can be written as superposition of bound states as $\sum_n b_n(t) \exp(-i\omega_n t)|n>$ for the B.I. attopulses. The coefficients satisfy $i\dot{b}_n(t) = \sum_m <n|V_{APT}(t)|m> b_m(t)$, where $|n>$ is the eigenket of $H_0(t) = \mathbf{p}^2/2 + V_a(r)$. Three major states $|1s>$, $|2p>$ and $|3p>$ in the SAE notation are considered with the APT considered in Fig. 1a. The system of coupled equations is solved numerically by the Runge–Kutta method.

With the initial partition of total Hamiltonian, the total wave function $|\Psi(t)>$ corresponding to $H(t)$ can be written as

$$|\Psi(t)> \, = |\varphi_i(t)> \, + \int_{t_i}^{t_f} dt_1 G(t, t_1) V_{IR}(t_1)|\varphi_i(t_1)>, \tag{3}$$

where $\left[i\frac{\partial}{\partial t} - H(t)\right]G(t, t') = \delta(t - t')$. The IR interaction $V_{IR}(t)$ can be expressed as

$$V_{IR}(t) = \frac{1}{c}\mathbf{A}_{IR}(t) \cdot \mathbf{p} + \frac{1}{2c^2}\mathbf{A}_{IR}^2(t), \tag{4a}$$

$$\mathbf{A}_{IR}(t) = \hat{z}\frac{cE_{IR}}{\omega_{IR}}\exp\left[-2\ln 2\left(\frac{t}{\tau_{IR}}\right)^2\right]\cos(\omega_{IR}t + \varphi_d), \tag{4b}$$

where $\tau_{IR} = 5\,fs$ is used unless otherwise specified. The IR frequency ω_{IR} is 1.55 eV. $\varphi_d \equiv -\omega_{IR}t_d$, with t_d being the time delay between the APT and IR field.

After the APT's excitation, the IR field becomes dominant in the final physical situation. Thus, the total Hamiltonian is then partitioned as $H(t) = H_f(t) + V_f(t)$, where $H_f = \mathbf{p}^2/2 + V_{IR}$ and $V_f = V_a + V_{APT}$. Let $\left[i\frac{\partial}{\partial t} - H_f(t)\right]G_f(t, t') = \delta(t - t')$. The total Green function is then expressed as

$$G(t, t') = G_f(t, t') + \int_{t_i}^{t_f} dt_1 G_f(t, t_1) V_f(t_1) G(t_1, t'), \tag{5}$$

where $G_f(t, t') = -i\Theta(t - t') \int d^3\mathbf{k}|\varphi_{f,\mathbf{k}}^V(t)> <\varphi_{f,\mathbf{k}}^V(t')|$, with $\Theta(t - t')$ being the step function and $\mathbf{k}$ the wave vector. The Volkov wave function $|\varphi_{f,\mathbf{k}}^V(t)>$ is given by
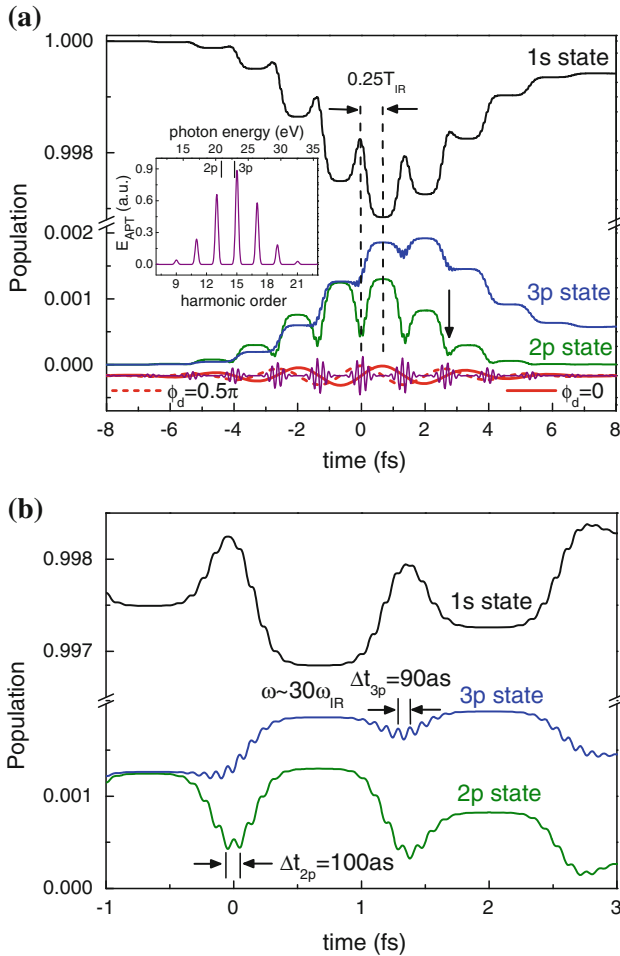
(a)

(b)

Fig. 1 (Color online) **a** Evolution of He ($1s$) in *black*, He ($2p$) in *green* and He ($3p$) in *blue*, labeled $|b_n(t)|^2$, excited by the B.I. attopulses without IR field, where $I_{APT} = 10^{13}$ W/cm^2, $\tau_x = 0.3$ fs, $\tau_T = 5$ fs and $\omega_x = 23$ eV. Schematic of the APT electric field (*violet*) is shown below. IR electric fields also shown below (*red solid line* for $\varphi_d = 0$ and *red dashed line* for $\varphi_d = 0.5\pi$) is used to elucidate the oscillation mechanism of ion yield. A time delay of about a one-quarter IR period between the plateau's center of population and the burst's peak of APT is illustrated. The *down arrow* indicates a local minimum of $2p$ or $3p$ population. *Inset* shows the spectrum of the B.I. APT. **b** Enlarged diagram for the CRW's oscillation in (**a**) with $\omega_{IR} = 1.55$ eV (800 nm)

$$\varphi_{f,\mathbf{k}}^V(t) = \varphi_{\mathbf{k}}(\mathbf{r}) \exp\left[-i\int\limits_{-\infty}^{t} E_{\mathbf{k}}(t')dt'\right], \qquad (6)$$

where $\varphi_{\mathbf{k}}(\mathbf{r}) = (2\pi)^{-3/2}\exp(i\mathbf{k}\cdot\mathbf{r})$. $E_{\mathbf{k}}(t) = \frac{1}{2}[\mathbf{k}+\mathbf{A}_{IR}(t)/c]^2$.

Substituting Eq. (5) into Eq. (3) yields the first-order transition amplitude

$$T_{\mathbf{k}}^{(b)}(t) = -i\int\limits_{t_i}^{t} dt_1 <\varphi_{f,\mathbf{k}}^V(t_1)|V_{IR}(t_1)|\varphi_i(t_1)>, \qquad (7)$$

where the second-order transition amplitude was neglected in our calculations [22].

In Eq. (2), the APT includes harmonics from H9 to H21 as shown in the inset of Fig. 1a, where H17, H19 and H21 are above the ionization threshold of He. The transition of the three harmonics from the ground state $|g>$ to the continuum state $|k>$ can be considered through the first-order time-dependent perturbation as

$$T_{\mathbf{k}}^{(a)}(t_f) = -i\int\limits_{t_i}^{t_f} dt_1 \exp(i\omega_{\mathbf{k}g}t_1) <\mathbf{k}|\mathbf{A}_{APT}^{(a)}(t_1)\cdot\mathbf{p}/c|g>$$

$$= -<\mathbf{k}|\hat{z}\cdot\mathbf{p}|g> F_{APT}^{(a)}(-\omega_{\mathbf{k}g})/\omega_{\mathbf{k}g}, \qquad (8)$$

where $\omega_{\mathbf{k}g} = \omega_{\mathbf{k}} - \omega_g$. $|\mathbf{k}> =i\exp[-i(\sigma_1+\delta_1)]R_{E1}(r)$ $Y_{10}(\Omega_{\mathbf{r}})Y_{10}^*(\Omega_{\mathbf{k}})$. The equation for the radial function $R_{E1}(r)$ is described in [9] and solved by using the Numerov method, except the fact that the momentum normalization is used as the Volkov wave uses it. σ_1 and δ_1 are the Coulomb and the short-range phase shifts, respectively. $Y_{10}(\Omega_{\mathbf{r},\mathbf{k}})$ is the spherical harmonics. $\mathbf{A}_{APT}^{(a)}(t)$ is the vector potential of $\mathbf{E}_{APT}^{(a)}(t)$. For the many-burst APT, $\mathbf{E}_{APT}^{(a)}(t) = \hat{z}E_x e^{-2\ln 2(t/\tau_T)^2}\sum_{n=17,19,21} a_n \sin(n\omega_{IR}t)$, where the amplitude a_n is determined by the corresponding Fourier component of $F_{APT}(\omega) = \int_{-\infty}^{\infty} E_{APT}(t)\exp(-i\omega t)dt$. For the few-burst APT, $\mathbf{E}_{APT}^{(a)}(t)$ is no longer fitted by the multi-peak Gaussian shape, and then a fully numerical model is needed, i.e., $F_{APT}^{(a)}(\omega) = F_{APT}(\omega)\Theta(\omega - I_p)$.

Thus, the photoelectron spectrum is given by

$$p(E) = \int\limits_{all\,\Omega_{\mathbf{k}}} \left|T_{\mathbf{k}}^{(b)}(t_f) + T_{\mathbf{k}}^{(a)}(t_f)\right|^2 kd\Omega_{\mathbf{k}}, \qquad (9)$$

Where $E = k^2/2$. Then, the ionization probability is calculated by $P = \int_0^\infty p(E)dE$.

2.2 HHG

Regarding the part of HHG, by constructing the wave function

$$|\Psi(t)> = |\varphi_i(t)> + \int d^3\mathbf{k} T_{\mathbf{k}}^{(b)}(t)|\varphi_{f,\mathbf{k}}^V(t)>, \qquad (10)$$

the dipole moment for harmonic emission can be expressed as

$$<\Psi(t)|z|\Psi(t)> = -i\int\limits_{t_i}^{t} dt_1 \int d^3\mathbf{k} <\varphi_i(t)|z|\varphi_{\mathbf{k}}>$$

$$<\varphi_{\mathbf{k}}|V_{IR}(t_1)|\varphi_i(t_1)>$$

$$\exp\left[-i\int\limits_{t_1}^{t} E_{\mathbf{k}}(t')dt'\right] + c.c., \qquad (11)$$

where we calculate the multiple integral accurately without using the stationary phase approximation [17]. c.c. is complex conjugate. The HHG spectrum is then given by

$$|HHG(\omega)|^2 = \left| \int_{-\infty}^{\infty} <\Psi(t)|z|\Psi(t)> \exp(-i\omega t)dt \right|^2 . \tag{12}$$

3 Results and discussions

3.1 Atomic ionization

Figure 1a shows the evolution of 1s, 2p and 3p states in helium, labeled $(|b_n(t)|^2)$, excited by the B.I. APT without the IR field. The schematic APT electric field is shown below (note that the IR electric fields shown in red will be used later). The population of bound states changes around each burst of APT. As each burst of APT passes, the 2p or 3p state reaches a local maximum plateau of population, while the 1s state reaches a local minimum plateau. The time delay between the center of the plateau of population and the peak of burst of APT is about one-quarter the IR period as depicted. As all bursts of APT have passed, the 3p population is higher than the 2p one because H15 of the APT is near resonant with the 3p state, as shown in the inset of Fig. 1a. Among these transitions, a very rapid oscillation is found. For better visualization, an enlarged diagram is shown in Fig. 1b. The oscillation time on the 3p state is as fast as 90 as ($\sim 30\omega_{IR}$) and exactly matched with $\omega_0(= \omega_{31}) + \omega_L(\approx 15\omega_{IR})$ of CRW's frequency. Although the APT consists of many harmonics, the nearest resonant behavior makes H15 most important among all frequencies of the APT in contributing to the CRW on the 3p state. Such oscillation also appears on other bound states. For the 2p state, the oscillation time (≈ 100 as) is slightly longer than that of the 3p state. This is reasonable because the CRW's frequency on the 2p state can be approximated by $\omega_0(= \omega_{21}) + \omega_L(\approx 13\omega_{IR})$. Interestingly, though the CRW's amplitude is small, it can cause a clear HHG, as shown later. Otherwise, the Rabi oscillation has negligible oscillation period at our used APT intensity that is three orders longer than that of CRW.

We investigate the effects of the IR field as shown in Fig. 1. Figure 2a shows the photoelectron spectra at different IR delay phases with $I_{IR} = 5 \times 10^{12}$ W/cm^2. As can be seen, a clear oscillation of photoelectron with the IR delay phase is illustrated. Integrating the photoelectron energy in Fig. 2a yields the ionization probability shown in Fig. 2b, where the blue solid and red dashed lines denote the results with and without the transition of H17 + H19 + H21, respectively. In both cases, an oscillation at a half IR

period coinciding with the experimental result [5] is shown. The maximum and minimum ionization probabilities are around $\varphi_d = \kappa\pi$ and $(\kappa + 0.5)\pi$, respectively, where κ is an integer. The mechanism can be explained with the help of Fig. 1a. For $\varphi_d = 0$, the peaks of the IR field [red solid line at the bottom of Fig. 1a] are aligned with the local maximum plateau of 2p or 3p population between two adjacent bursts of APT (the ionization from the 1s state is very weak and can be neglected). Thus, the IR field has the strongest ionization efficiency. On the other hand, for $\varphi_d = 0.5\pi$, the peaks of IR field [red dashed line at the bottom of Fig. 1a] shift to the local minimum of 2p or 3p population as the down arrow indicates. In other words, the local maximum plateau of 2p or 3p population becomes aligned with the zero of the IR field. Thus, its ionization efficiency becomes the weakest. Due to spherical symmetry of the atom, the positive and negative IR cycles have the same effect on the photoelectron ionization. Thus, the
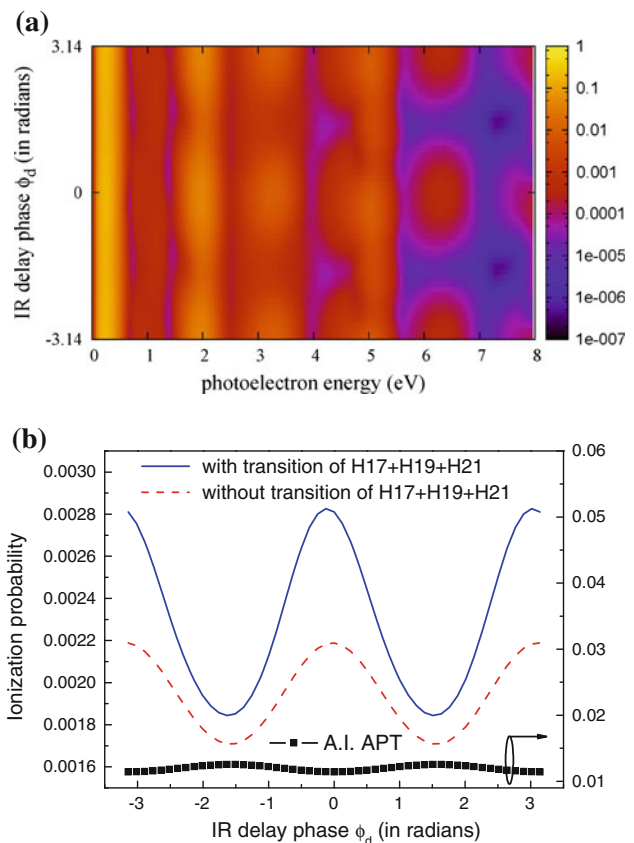

Fig. 2 (Color online) **a** Photoelectron spectra in He as a function of IR delay phase with the bound-state population in Fig. 1a driven by $I_{IR} = 5 \times 10^{12}$ W/cm^2, where the APT is assumed to be strong enough to let the population remain on the bound states. **b** Ionization probability from (**a**) as a function of IR delay phase. *Blue solid and red dashed lines* denote the results with and without the transition of H17 + H19 + H21, respectively. Scatter denotes the result excited by A.I. APT and IR with the theory [9]

oscillation of ionization probability is in a one-half IR period. Here, including the transition of H17 + H19 + H21, simply called A.H. (above harmonics) later, does not destroy the oscillation, but increases the ionization probability. The A.H. transition does not depend on the IR delay phase, while the transition from $2p$ to $3p$ states does. Thus, the two-path interference can be constructive or destructive as the IR phase varies, which makes the enhancement of ionization strong around $\varphi_d = \kappa\pi$ and weak around $(\kappa + 0.5)\pi$. Otherwise, if the central energy of APT is above the ionization potential, the IR field acts as the streaking effect and the oscillation disappears as shown by the scatter, where ω_X is set to 35 eV [9]. The result agrees with the experimental findings of Johnsson et al. [5].

The aligned effect (between the population plateau and the IR field) is a different mechanism from the interference effect by the APT's bursts. Both the effects exist in the IR-driven atomic ionization assisted by the B.I. APT. However, the aligned effect can explain why the oscillation still exists even if a few-burst APT is excited. In contrast, the interference effect by the APT's bursts can reshape the oscillation pattern of ionization probability. To elucidate this point, we plot Fig. 3a for the photoelectron spectra excited by APTs that contain distinct burst's numbers, where $I_{\text{IR}} = 5 \times 10^{12}$ W/cm^2 and $\tau_{IR} = 5fs$. The left and right panels of Fig. 3b show the ionization probabilities with and without the A.H. transition, respectively. First, we can see that the oscillation of ionization probability exists even for the SAP. Next, as the burst's number increases, the interference effect increases and leads to a multi-peak structure in the photoelectron spectra. The swing of ionization probability ($P_{\text{max}} - P_{\text{min}}$) also increases consequently, and the IR delay phase where the maximum ionization probability takes place shifts to $\kappa\pi$ gradually.
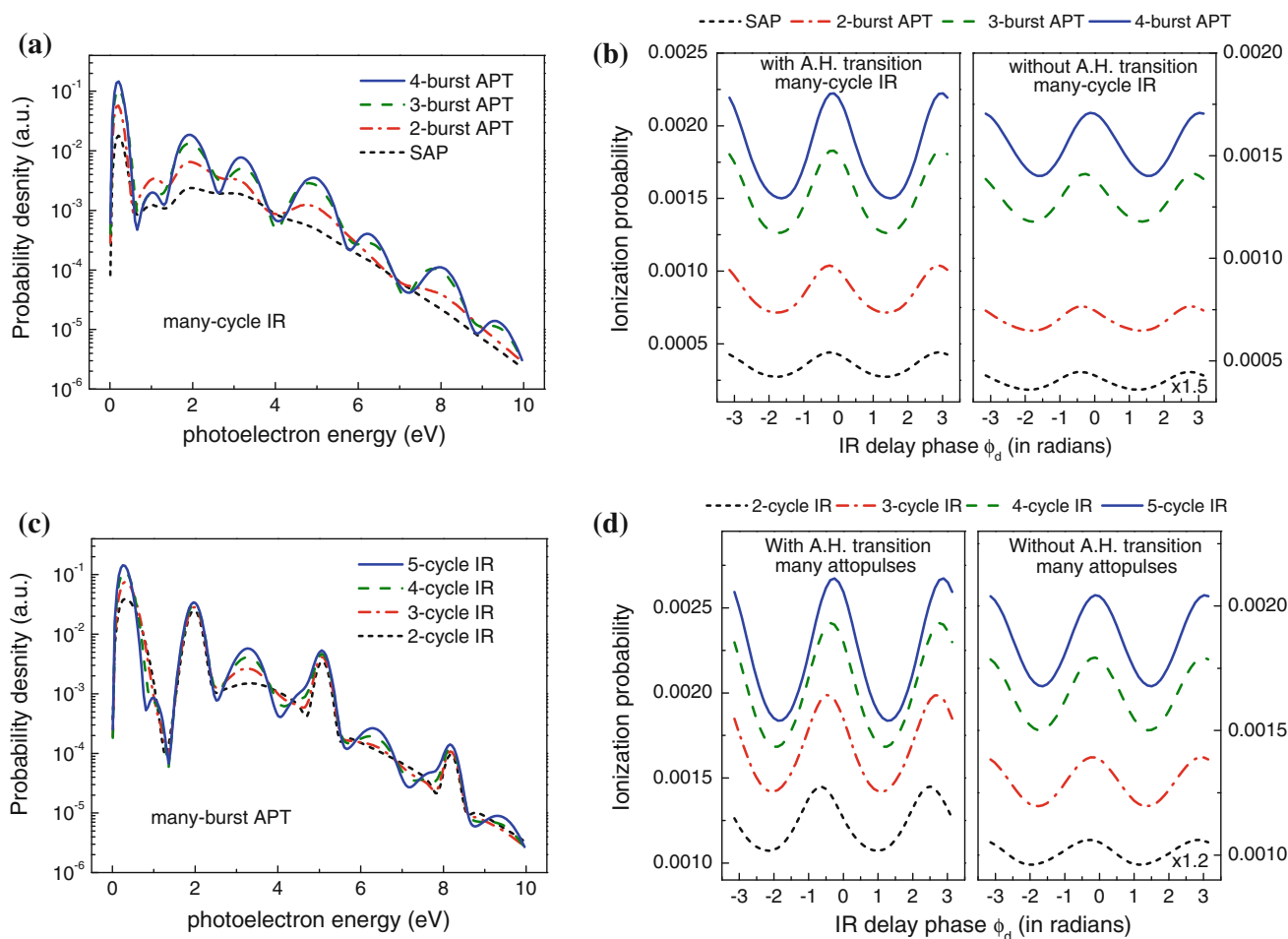

Fig. 3 (Color online) a Photoelectron spectra in He excited by few-burst B.I. APT + many-cycle IR at $I_{\text{IR}} = 5 \times 10^{12}$ W/cm^2 and $\varphi_d = 0$. Blue solid, green dashed, red dash-dotted and black dotted lines denote the results of 4-, 3-, 2-burst APT, and SAP, respectively. b Ionization probability from (a) as a function of IR delay phase with (left) and without (right) the A.H. (above harmonic) transition.

c Photoelectron spectra in He excited by few-cycle IR + many-burst B.I. APT at $I_{\text{IR}} = 5 \times 10^{12}$ W/cm^2 and $\varphi_d = 0$. Blue solid, green dashed, red dash-dotted and black dotted lines denote the results of 5-, 4-, 3-cycle and 2-cycle IR, respectively. d Ionization probability from (c) as a function of IR delay phase with (left) and without (right) the A.H. transition

Third, at a higher IR intensity such as 10^{13} W/cm^2, the modulation ratio $(P_{max} - P_{min})/(P_{max} + P_{min})$ can increase with the burst's number, because the increase of $(P_{max} + P_{min})$ with the burst's number begins to saturate.

This point is also supported by the few-cycle IR excitation. Figure 3c shows the photoelectron spectra excited by the IR fields that contain distinct optical cycles at $I_{IR} = 5 \times 10^{12}$ W/cm^2 along with many-burst APT (ξ from -10 to 10). The left and right panels of Fig. 3d show the ionization probabilities with and without the A.H. transition, respectively. The oscillation exists even for few-cycle IR, where the interference effect is weak. As the IR-cycle number increases, the interference effect is increasingly strong and causes a multi-peak structure in the photoelectron spectra. Note that the peaks around 2, 5 and 8 eV come from the H17, H19 and H21, respectively, and thus they are not affected by the IR-cycle number. The swing of ionization probability increases and the IR delay phase with maximum ionization probability shifts to $\kappa\pi$ gradually. At a higher IR intensity (10^{13} W/cm^2), the modulation ratio also increases with the IR-cycle number in our calculation. Incidentally, the ponderomotive shift for the A.H. transition is only 2×10^{-3} eV, while the shift for the IR-driven ionization from $3p$ or $2p$ state is about 0.3 eV. Thus, the spacing between the two groups of transitions slightly deviates from the IR energy.

In the above discussions, the APT intensity is supposed to be strong enough to let the population of Fig. 1a remain on the bound states. The assumption may be relieved by considering the depletion effect of bound states within the ADK theory [23]. However, while the ADK theory was applied, we found that it overestimated the ionization rate of $2p$ and $3p$ states greatly and made the results incompatible with those experimentally found [5]. Thus, a more accurate depletion calculation is required in the future. Meanwhile, the assumption of strong enough APT should be adequate. We will show that the assumption still holds [8] even at a 100 times higher IR intensity, which does not make the result too different from the experimental data [8]. Thus, the mechanism presented should not be affected by the assumption of a modest IR intensity.

Generally, the S-matrix theory is not gauge invariant [24–35] due to the fact that only the first-order term is kept [36, 37] or the strong field approximation is made. The gauge-induced difference could be quantitative [9, 24–26] or qualitative [27–35]. In some situations, the velocity-gauge (VG) results can agree with experimental results or provide a better description of relative physical processes [18, 25, 34, 35, 38, 39], while in some cases, the length gauge (LG) is better than the VG in predicting theoretical results [24, 27–29, 31–33]. Our theory described in Sect. 2 and results shown earlier are under VG. We now study the gauge effect in the case of LG.
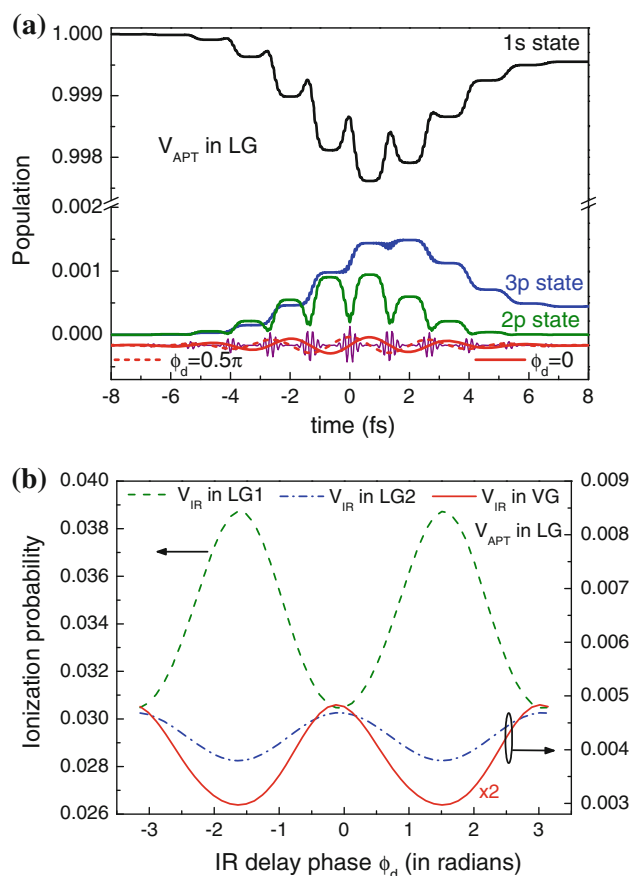

Fig. 4 (Color online) Gauge analysis. **a** As in Fig. 1a, but with $V_{APT}(t)$ calculated under the length gauge (LG). **b** Ionization probability from (**a**) with $V_{IR}(t)$ calculated under the VG (*red solid line*), the first length gauge (LG1 in *green dashed line*) and the second length gauge (LG2 in *blue in dashed-dotted*) as a function of IR delay phase at $I_{IR} = 5 \times 10^{12}$ W/cm^2 with the A.H. transition

First of all, $|\varphi_i(t)>$ is re-calculated by $V_{APT}^{(LG)}(t) = \mathbf{r} \cdot \mathbf{E}_{APT}(t)$ and shown in Fig. 4a. The result is qualitatively the same as that in Fig. 1a. The population of bound states changes around each burst of APT. As each burst passes, the excited bound (ground) states reach a local maximum (minimum) plateau. The rapid oscillation caused by the CRW is also shown. Quantitatively, there is a slight difference between the two gauges, because only three bound states that are nearly resonant by the H13 and H15 are included in $|\varphi_i(t)>$, while the A.H. transition is considered by Eq. (8), which is also transferred to the LG and an agreement with the VG can be obtained. Next, using the LG-based $|\varphi_i(t)>$, the ionization probability for distinct conditions with the A.H. transition is shown in Fig. 4b. If $V_{IR}(t)$ in Eq.(7) remains under VG, the ionization probability (denoted by the red solid line) can demonstrate the same oscillation dependence as that in Fig. 2b. If Eq. (7) is further transformed to the LG as

$$T_{\mathbf{k}}^{(b)} = -i \int_{-\infty}^{\infty} dt < \varphi_{f,\mathbf{k}+\mathbf{A}_{IR}(t)/c}^{V}(t) | \mathbf{r} \cdot \mathbf{E}_{IR}(t) | \varphi_i(t) > , \quad (13)$$

the result (denoted by the green dashed line) also shows the oscillation with one-half IR period, but the oscillation has an out-of-phase difference from that in Fig. 2b [40]. The difference is due to insufficient order terms considered in the S matrix. Under the first-order-term calculation, since $\mathbf{E}_{IR}(t)$ has a 0.5 π phase shift from $\mathbf{A}_{IR}(t)$, the local maximum plateau of $2p$ or $3p$ population aligned with the peak of IR field under the VG now becomes aligned with the zero of IR field under the LG. Thus, the maximum ionization probability turns to the minimum, and vice versa (min. to max.). If enough higher-order terms are taken, the two gauges give a consistent result [36, 37]. On the other hand, the contradiction may be eliminated by expressing the LG transition amplitude to another form [41–45]. In Eq. (13), one can rewrite $\mathbf{r} \cdot \mathbf{E}_{IR}(t)$ as $H_f - H_i + V_a + V_{APT} = -i\overleftarrow{\partial}_t - i\overrightarrow{\partial}_t + V_a + V_{APT}$. Via integration by parts, Eq. (13) becomes $-i \int_{-\infty}^{\infty} dt \Big[< \varphi_{f,\mathbf{k}+\mathbf{A}_{IR}(t)/c}^{V}(t) | V_a + V_{APT} | \varphi_i(t) > + < \varphi_{f,\mathbf{k}+\mathbf{A}_{IR}(t)/c}^{V}(t) | \sum_n \dot{b}_n(t)\varphi_n(t) > \Big]$. By writing $V_a + V_{APT}$ as $\nabla^2/2 + (-\nabla^2/2 + V_a + V_{APT})$, the first term can be applied to the Volkov wave and the second term to the $|\varphi_i(t) >$ [46]. Eventually, we obtain

$$T_{\mathbf{k}}^{(b)} = -i \int_{-\infty}^{\infty} dt \sum_n b_n(t) < \varphi_{f,\mathbf{k}+\mathbf{A}_{IR}(t)/c}^{V}(t) | \varphi_n(t) >$$
$$\left[-\frac{1}{2}\left(\mathbf{p} + \frac{1}{c}\mathbf{A}_{IR}(t)\right)^2 + \omega_n \right]. \quad (14)$$

If a factor $\exp[-i\mathbf{A}_{IR}(t) \cdot \mathbf{r}/c]$ is further inserted into the integral in Eq. (14), the oscillation pattern (denoted by blue dashed-dotted line called LG2) can recover to the same dependence on the IR delay phase as that of VG, while the result based on Eq. (13) called LG1 in Fig. 4b cannot do that even in the presence of the factor. The VG result agrees with the TDSE result [10, 47] at IR intensities below 7×10^{12} W/cm^2. Their maximum ionization probability takes place at the IR phase of $(\kappa + 0.5)\pi$ in contrast to ours ($\kappa\pi$), because they use a cosine electric field while we use a cosine wave for the IR vector potential. At IR intensities above 10^{13} W/cm^2, the TDSE result [47] shows an out-of-phase oscillation as compared to that at intensities below 7×10^{12} W/cm^2. Thus, our LG1 result in Fig. 4b becomes consistent with the TDSE result [47] as well as the experimental result [5] (from the intensity 5×10^{12} to 10^{13} W/cm^2, the LG1 oscillation dependence on the IR phase remains the same, and so does VG). In this situation, if the factor $\exp[i\mathbf{A}_{IR}(t) \cdot \mathbf{r}/c]$ is inserted into the integral in

Eq. (7), the VG result can be converted to have the same IR-phase dependence as that of LG1, where the gauge contradiction can be avoided accordingly. Since our definition of IR phase is the same as that in the experimental result [5], the two works show that the maximum ionization probability takes place at $(\kappa + 0.5)\pi$.

Our explanation for the ionization oscillation is, in principle, equivalent to the mechanism of Tong et al. [10] though the two representations seem quite different. In their work [10], atomic structures in an IR laser are described by the Floquet states. Extremely ultraviolet (XUV) transition in atom thus makes interference among these Floquet states, where both SAP and APT can result in the oscillation of photoelectron spectra with the IR delay phase at a narrow energy range. This is consistent with our argument that the aligned effect explains the ionization oscillation caused by the SAP. Next, the APT has a narrower energy bandwidth than the SAP, and thus corresponding Floquet states are fewer than those of SAP. As a result, few Floquet states for the APT make interference coherent and then the ionization probability is sensitive to the IR delay phase. The argument is similar to ours, but becomes the version of time domain, i.e., an increased attopulse's number makes the interference effect strong and enhances the swing of ionization probability. As we can see, their explanation is essentially based on the energy representation (interference among Floquet states), while ours is based on the time representation (interference among attopulses). The two distinct approaches, however, can give the same prediction for the oscillation phenomenon.

3.2 HHG

Figure 5a shows the harmonic spectrum caused by the bound-state population in Fig. 1a driven with an IR field of 10^{13} W/cm^2. Three distinct groups are shown in the harmonic spectrum. We use the schematic diagram in Fig. 5b to elucidate its origin. Atomic electrons are first excited by the B.I. APT and then ionized by the IR field. Due to the IR field, the ionized electrons leave, turn around, accelerate and finally recombine with their parent ions via multichannels. The left-hand side group ($<8\omega_{IR}$) is related to the recombination to $2p$ and $3p$ states immersed in the perturbative region of HHG, which rapidly decreases with increased harmonic order. The middle group ($\sim 16\omega_{IR}$) corresponds to the recombination to $1s$ state. As mentioned above, the CRW causes a rapid oscillation on the three bound states in Fig. 1b. The right-hand side group ($\sim 30\omega_{IR}$) is related to the CRW-induced spectrum. The spectrum is not weak, and thus provides a way to identify the rapid oscillation of bound-state population. In addition, the spectrum varies as the IR delay phase changes: strong around $\varphi_d = \kappa\pi$, but weak around $\varphi_d = (\kappa + 0.5)\pi$. This
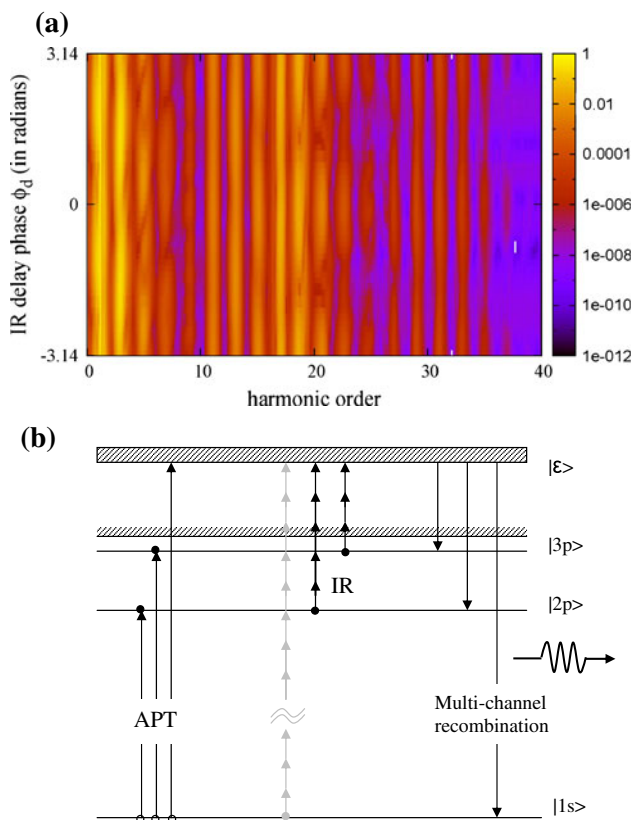
(a)

(b)

Fig. 5 (Color online) **a** Harmonic spectra from He as a function of IR delay phase with the bound-state population in Fig. 1a at $I_{IR} = 10^{13}$ W/cm^2, where the APT intensity is supposed to be strong enough to let the population remain on the bound states. **b** Schematic diagram of multi-channel recombination and dramatic enhancement of HHG from He excited by the B.I. APT first and then ionized by an IR field

dependence coincides with the photoelectron spectra shown in Fig. 2a, which thus reconfirms the aligned effect described earlier.

In Fig. 5a, it is difficult to distinguish the recombination to $2p$ (or $3p$) state from the perturbative region of HHG. To clarify this point, we consider the spectrum accomplished through only the $2p$ state, i.e., only $|2p>$ was counted in $\varphi_i(t_1)$ and $\varphi_i(t)$ and written in Eq. (11), whose result is shown in Fig. 6a. Black scatter and red solid line denote the result of $I_{IR} = 10^{13}$ and 10^{14} W/cm^2, respectively. As the IR intensity increases, we can see that the left-hand-side group extends a high-order harmonic plateau. The cutoff energy ω_c is about $15\omega_{IR}$ and this matches with $I_p^{(2p)} + 3.17U_p$ given by the three-step model, where $I_p^{(2p)} = 0.13$ (a.u.) is the ionization potential from the $2p$ state and $U_p = E_{IR}^2/(4\omega_{IR}^2)$ is the ponderomotive energy. For comparison, we show Fig. 6b for the spectrum accomplished through only the $1s$ state, which shows no
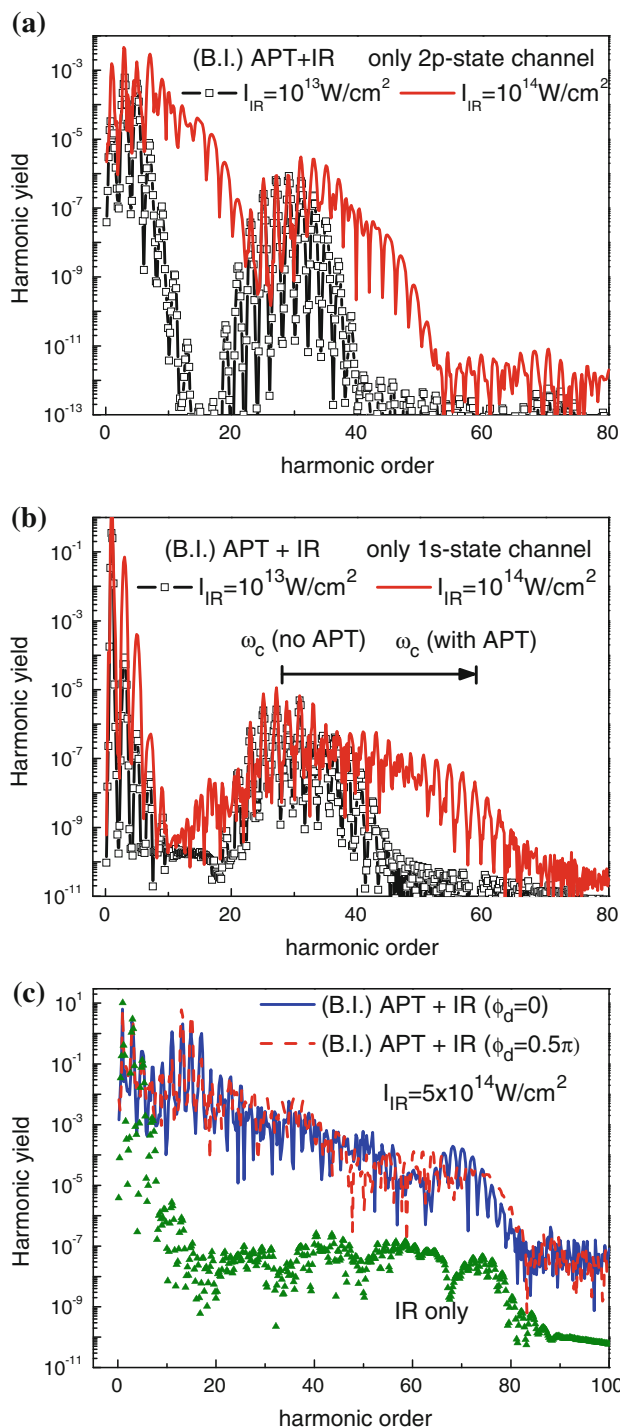
(a)

(b)

(c)

Fig. 6 (Color online) **a** HHG spectra from He excited by the B.I. APT + IR ($\varphi_d = 0$) through only the $2p$-state channel at $I_{IR} = 10^{13}$ W/cm^2 (*black square* scatter) and $I_{IR} = 10^{14}$ W/cm^2 (*red solid line*), where only $|2p>$ is counted in $\varphi_i(t_1)$ and $\varphi_i(t)$ is written in Eq. (11). **b** HHG spectra from He excited by the B.I. APT + IR ($\varphi_d = 0$) through only the $1s$-state channel with the same symbolic meanings as those in (**a**). **c** HHG spectra from He excited by the B.I. APT + IR field at $\varphi_d = 0$ (*blue solid line*) and $\varphi_d = 0.5\pi$ (*red dashed line*), and by the IR only (*green triangular* scatter) show a dramatic enhancement of HHG, where $I_{IR} = 5 \times 10^{14}$ W/cm^2

such plateau. Therefore, the left-hand side group shown in Figs. 5a and 6a indeed consists of recombination to the $2p$ state. The same deduction holds for the case of the $3p$ state; we do not show its result again.

Interestingly, from Fig. 6a, b, we find that the CRW's spectrum also has a high-order harmonic plateau as the IR intensity increases. The CRW's cutoff energy from the $1s$ state is about $60\omega_{IR}$, which is broader than that from the $2p$ state of about $50\omega_{IR}$. Both the values are larger than $I_p^{(CRW)} + 3.17U_p = 42\omega_{IR}$, i.e., when $I_p^{(CRW)} = 30\omega_{IR}$ (CRW's central frequency). This implies that the plateau's mechanism should be different from that of the three-step model. On the other hand, due to the extra spectrum caused by the CRW, the overall harmonic spectrum also no longer satisfies the usual rule of $\omega_c = I_p^{(1s)} + 3.17U_p$ estimated by the three-step model. At $I_{IR} = 10^{14}$ W/cm^2, the cutoff energy is $28\omega_{IR}$ in the absence of the B.I. APT as indicated in Fig. 6b, but becomes $60\omega_{IR}$ once the B.I. APT is included. Thus, the presence of the B.I. APT makes invalid the usual rule of cutoff frequency driven by the IR field.

Besides the CRW spectrum, another interesting effect of the B.I. APT is the dramatic enhancement of HHG [8, 19, 20]. The reason is comprehensible. Due to the APT, some electrons occupy the $2p$ and $3p$ states. The ionization from $2p$ or $3p$ state is much easier than that from $1s$ state for they are much closer to the continuum states. Thus, the HHG assisted by the B.I. APT is enhanced significantly. To compare with the experimental result [8], we show the HHG spectra at $I_{IR} = 5 \times 10^{14}$ W/cm^2 in Fig. 6c, where the APT intensity is again supposed to be strong enough to keep $2p$ and $3p$ populations. The 27th harmonic order in the presence of the APT field (blue solid line for $\varphi_d = 0$ and red dashed line for 0.5π) is about 10^4 times higher than that of IR alone (green scatter). The factor is only 2.5 times larger than that experimentally found (4×10^3) [8], but if the ADK theory is applied to the depletion effect, $2p$ and $3p$ states deplete entirely at the IR intensity, making the calculations incompatible with the experimental result [8]. Consequently, while the model without the depletion effect is crude, it still captures a qualitative description of the dramatic HHG's enhancement.

4 Conclusion

In conclusion, we apply the IMST to elucidate the control mechanism of atomic ionization excited by the B.I. attopulse along with IR fields. For $\varphi_d = 0$ (bursts of APT coincided with zero of the IR field), the local maximum plateau of $2p$ or $3p$ population created by the attopulses is aligned with the peaks of IR field well, thus leading to a strongest ionization at IR intensities below 7×10^{12} W/cm^2. For $\varphi_d = 0.5\pi$

(bursts of APT coincided with peaks of IR field), the local maximum plateau of $2p$ or $3p$ population, however, shifts to zero of IR field, and hence the ionization is weakest at IR intensities below 7×10^{12} W/cm^2. Atomic symmetry makes the oscillation in one-half IR period. Due to the aligned effect, the ionization oscillation is robust even for a few-burst APT or a few-cycle IR field. On the other hand, the interference among successive EWPs caused by the APT becomes strong as the burst's number or the IR cycle increases and then reshapes the oscillation pattern. The aligned and interference effects give a clear explanation for the ion-yield oscillation in time representation.

The B.I. attopulses also produce several evident effects on the HHG (the CRW's spectrum, dramatic enhancement of HHG and multi-channel recombination). First, the CRW created by the B.I. attopulses coupled to atomic states causes a rapid oscillation on the bound states. By applying an IR field, the rapid oscillation can result in a clear harmonic emission, which also has a high-order plateau as the IR intensity increases. The CRW's spectrum provides a way to detect the rapid oscillation of the bound states. Next, the B.I. attopulses make some electrons occupy the excited bound states. These excited electrons are easily ionized by the IR field and lead to a considerable amount of continuum electrons. Thus, the HHG is dramatically enhanced. The idea is likely implemented combined with other methods, such as supercontinuum generation [48, 49] to produce an intense SAP. Finally, due to the presence of excited bound electrons, the continuum electrons can recombine with their parent ions not only via the ground state, but also via these excited bound states. A multi-channel recombination thus takes place and provides another method to generate a variety of optical sources.

References

1. F. Krausz, M. Ivanov, Rev. Mod. Phys. **81**, 163 (2009)
2. H.G. Muller, Appl. Phys. B **74**, S17 (2002)
3. Y. Mairesse, A. Bohan, L.J. Frasinski, H. Merdji, L.C. Dinu, P. Monchicourt, P. Breger, M. Kovačev, R. Taieb, B. Carré, H.G. Muller, P. Agostini, P. Salières, Science **302**, 1540 (2003)
4. P. Johnsson, R. López-Martens, S. Kazamias, J. Mauritsson, C. Valentin, T. Remetter, K. Varjú, M.B. Gaarde, Y. Mairesse, H. Wabnitz, P. Salières, P. Balcou, K.J. Schafer, A. L'Huillier, Phys. Rev. Lett. **95**, 013001 (2005)
5. P. Johnsson, J. Mauritsson, T. Remetter, A. L'Huillier, K.J. Schafer, Phys. Rev. Lett. **99**, 233001 (2007)
6. C.F. De Morrison Faria, P. Salières, P. Villain, M. Lewenstein, Phys. Rev. A **74**, 053416 (2006)
7. C.F. De Morisson Faria, P. Salières, Laser Phys. **17**, 390 (2007)

8. E.J. Takahashi, T. Kanai, K.L. Ishikawa, Y. Nabekawa, K. Midorikawa, Phys. Rev. Lett. **99**, 053904 (2007)
9. H.C. Lee, S.D. Jheng, T.F. Jiang, J. Opt. Soc. Am. B **29**, 286 (2012)
10. X.M. Tong, P. Ranitovic, C.L. Cocke, N. Toshima, Phys. Rev. A **81**, 021404(R) (2010)
11. F. Kelkensberg, W. Siu, J.F. Pérez-Torres, F. Morales, G. Gademann, A. Rouzée, P. Johnsson, M. Lucchini, F. Calegari, J.L. Sanz-Vicario, F. Martín, M.J.J. Vrakking, Phys. Rev. Lett. **107**, 043002 (2011)
12. S.I. Chu, D.A. Telnov, Phys. Rep. **390**, 1 (2004)
13. L.Y. Peng, E.A. Pronin, A.F. Starace, New J. Phys. **10**, 025030 (2008)
14. P. Ranitovic, X.M. Tong, B. Gramkow, S. De, B. DePaola, K.P. Singh, W. Cao, M. Magrakvelidze, D. Ray, I. Bocharova, H. Mashiko, A. Sandhu, E. Gagnon, M.M. Murnane, H.C. Kapteyn, I. Litvinyuk, C.L. Cocke, New J. Phys. **12**, 013008 (2010)
15. P. Rivière, O. Uhden, U. Saalmann, J.M. Rost, New J. Phys. **11**, 053011 (2009)
16. P.B. Corkum, Phys. Rev. Lett. **71**, 1994 (1993)
17. M. Lewenstein, P. Balcou, M.Y. Ivanov, A. L'Huillier, P.B. Corkum, Phys. Rev. A **49**, 2117 (1994)
18. A. Becker, F.H.M. Faisal, J. Phys. B **38**, R1 (2005)
19. K.L. Ishikawa, Phys. Rev. Lett. **91**, 043002 (2003)
20. D.B. Milošević, J. Opt. Soc. Am. B **23**, 308–317 (2006)
21. X.M. Tong, C.D. Lin, J. Phys. B **38**, 2593 (2005)
22. Z. Chen, T. Morishita, A.T. Le, C.D. Lin, Phys. Rev. A **76**, 043402 (2007)
23. N.B. Delone, V.P. Krainov, *Multiphoton processes in atoms* (Springer, Berlin, 1994), pp. 66–80
24. B. Bergues, Y. Ni, H. Helm, I.Yu. Kiyan, Phys. Rev. Lett. **95**, 263002 (2005)
25. H.R. Reiss, Phys. Rev. A **76**, 033404 (2007)
26. J. Zhang, T. Nakajima, Phys. Rev. A **77**, 043417 (2008)
27. B. Bergues, Z. Ansari, D. Hanstorp, I.Yu. Kiyan, Phys. Rev. A **75**, 063415 (2007)
28. J.H. Bauer, Phys. Rev. A **85**, 063417 (2012)
29. J.H. Bauer, J. Phys. B **41**, 185003 (2008)
30. J. Zhang, T. Nakajima, Phys. Rev. A **75**, 043403 (2007)
31. D. Bauer, D.B. Milošević, W. Becker, Phys. Rev. A **72**, 023415 (2005)
32. Y.J. Chen, B. Hu, Phys. Rev. A **80**, 033408 (2009)
33. T.K. Kjeldsen, L.B. Madsen, J. Phys. B **37**, 2033 (2004)
34. C.C. Chirilă, M. Lein, Phys. Rev. A **73**, 023410 (2006)
35. A.S. Kheifets, I. Bray, Phys. Rev. A **57**, 2590 (1998)
36. F.H.M. Faisal, Phys. Rev. A **75**, 063412 (2007)
37. F.H.M. Faisal, J. Phys. B **40**, F145 (2007)
38. H.R. Reiss, Phys. Rev. A **77**, 067401 (2008)
39. H.R. Reiss, Phys. Rev. A **54**, R1765 (1996)
40. L.B. Madsen, D. Dimitrovski, Phys. Rev. A **78**, 023403 (2008)
41. W. Becker, F. Grasbon, R. Kopold, D.B. Milošević, G.G. Paulus, H. Walther, Adv. At. Mol. Opt. Phys. **48**, 35 (2002)
42. M.H. Mittleman, *Introduction to the theory of laser-atom interactions* (Plenum press, New York, 1993), p. 192
43. H.R. Reiss, Prog. Quantum Electron. **16**, 1 (1992)
44. D.B. Milošević, F. Ehlotzky, Phys. Rev. A **57**, 5002 (1998)
45. H. R. Reiss, in *Atoms in Strong Fields*, vol. 212, ed. by C. A. Nicolaides, C. W. Clark, M. H. Nayfeh (Plenum Press, New York, 1990), p. 425
46. A. Gazibegović-Busuladžić, D.B. Milošević, W. Becker, Opt. Commun. **275**, 116 (2007)
47. X.M. Tong, N. Toshima, Phys. Rev. A **81**, 043429 (2010)
48. J.G. Chen, Y.J. Yang, S.L. Zeng, H.Q. Liang, Phys. Rev. A **83**, 023401 (2011)
49. G.T. Zhang, X.S. Liu, J. Phys. B **42**, 125603 (2009)